**Electronic supplementary information (ESI)**

# Construction of honeycomb-like Te-doped NiCo-LDHs for aqueous supercapacitors and as oxygen evolution reaction electrocatalysts

Ding Zhang[a,b,c], Xiaoning Tang[d], Zhaoguang Yang[a,b], Ying Yang[a*], Haipu Li[a,b*]

a. *College of Chemistry and Chemical Engineering, Central South University, Changsha 410083, PR China*

*b. Key Laboratory of Hunan Province for Water Environment and Agriculture Product Safety,* Changsha 410083, *PR China*

*c. School of Chemistry and Chemical Engineering, Hainan Normal University, Haikou Hainan 571158, PR China*

*d. Faculty of Chemical Engineering, Kunming University of Science and Technology, Kunming Yunnan 650500, PR China*

***Corresponding authors.**

**E-mail addresses:** yangy@csu.edu.cn (Ying Yang), lihaipu@csu.edu.cn (Haipu Li)

# Content

## Preparation of electrode materials

Chemicals: nickel(II) nitrate ($Ni(NO_3)_2 \cdot 6H_2O$, ≥98%), cobalt(II) nitrate ($Co(NO_3)_2 \cdot 6H_2O$, ≥98.5%), tellurium dioxide ($TeO_2$, ≥99.99%), sodium carbonate ($Na_2CO_3$, ≥99.8%), sodium bicarbonate ($NaHCO_3$, ≥99.5%), $NH_4F$ (≥98%), $(NH_4)_2SO_4$ (≥99.5%), glycol (≥99%), glycerol (≥99%) and potassium hydroxide (KOH, 95%) were obtained from Shanghai Aladdin Bio-Chem Technology Co., Ltd. All electrolyte solutions were prepared using ultrapure water (18.2 MΩ). The high concentration of carbonate and hydrocarbonate solution of pH 10.7 was prepared by mixing $Na_2CO_3$ and $NaHCO_3$ ($[CO_3^{2-}] + [HCO_3^-] = 2$ mol $L^{-1}$) in 100 mL ultrapure water.

Before electrodeposition, the NF substrate (20×10×2 $mm^3$) was sequentially ultrasonically cleaned by alcohol, acetone, trichloroethylene, and ultrapure water. Firstly, the NF substrate was anodized at 2 V (vs Ag/AgCl) in an electrolyte containing fluorine (1 mol $L^{-1}$ $NH_4F$ as corrosion and punching agent, 1 mol $L^{-1}$ $(NH_4)_2SO_4$, 15 mL glycol, 15 mL glycerol as a leveling agent and 70 mL ultrapure water) for 2 h. The anodic oxidation process can be demonstrated by eq. (S1).[1]

$$Ni + 2H_2O \rightarrow Ni(OH)_2 + 2H^+ + 2e^- \quad \text{(S1a)}$$

$$Ni(OH)_2 \rightarrow NiO + H_2O \quad \text{(S1b)}$$

Then the pre-anodized NF (NiO/NF) was selected as the working electrode, platinum plating titanium mesh as the counter electrode, and Ag/AgCl (saturated KCl) as the reference electrode in the three-electrode workstation and treated by potentiodynamic polarization from 0.2 to 1.2 V (vs Ag/AgCl). In the anodic oxidation

system, the $F^-$ ions from $NH_4F$ played an important role as corrosion and punching agent during the anodization process, and it promoted the formation of NiO.[2] On the other hand, the high viscosity glycerol/glycol solution provided the basis for the smooth and uniform anodic oxidation reaction, thus obtaining the porous structure with ideal morphology and thickness.[2, 3]

The preparation parameters were optimized by a series of single-factor experiments concerning initial concentrations of $Ni(NO_3)_2$ (0.5, 1 and 2 mmol $L^{-1}$), $Co(NO_3)_2$ (1, 2 and 2.5 mmol $L^{-1}$), $TeO_2$ (0.1, 0.2, 1 and 2 mmol $L^{-1}$), and electroplating times (50, 100, 200 and 500 s) (Figure S1, Supporting Information). The title electrode (denoted as HS-Te-NiCo-LDH/NiO/NF) was manufactured under the optimal condition: 1 mmol $L^{-1}$ $Ni(NO_3)_2$, 0.1 mmol $L^{-1}$ $TeO_2$, and 2 mmol $L^{-1}$ $Co(NO_3)_2$ and 200 s electroplating times (Figure S1f). In the potential range of 0.2 to 0.9 V (vs Ag/AgCl), the low current density could mainly allow for the completion of slow nucleation of HS-Te-NiCo-LDH, while the oxygen evolution was negligible. In the range above 0.9 V (vs Ag/AgCl), the dynamic oxygen bubbles were increasingly formed by OER and they functioned as the pore-forming reagents to affect the electrodeposition sites of metal hydroxides on the electrode surface during their bubble lifecycle of formation, growth, and detachment.[4]

For comparison reasons, control samples with or without Te doping, with or without LDH character (Te-NiFe-LDH/NiO/NF, HS-NiCo-LDH/NiO/NF; Te-NiOH/NiO/NF, Te-CoOH/NiO/NF, Te-NiMnOH/NiO/NF, Te-NiCuOH/NiO/NF),

and with or without NiO bottom layer (Te-NiOH/NiO/NF, Te-NiCo-LDH/NF) were prepared. The control tests were carried out in Figure S1 (Supporting Information).

**XRD, SEM, TEM, and XPS Characterization**

The morphology and the composition of the obtained materials were investigated using a scanning electron microscope (SEM) (Philip XL-40FEG) with EDS (EDAS NOVA NANOSEM 450), TEM (Tecnai G2 F20 S-TWIN) and X-ray photoelectron spectroscopy (XPS) (ESCALAB 250Xi, Thermo Fisher). The phase and crystallinity were examined by X-ray diffraction (XRD) using Cu Kα as the radiation (Bruker D8 ADVANCE A25X).

**Electrochemical measurement**

OER Tests.

Electrocatalytic activity of the synthesized electrocatalyst toward OER was evaluated using an electrochemical workstation (CS310, Wuhan CorrTest Instruments Corp., Ltd.) in 1.0 and 0.1 mol $L^{-1}$ KOH solutions by linear sweep voltammetry (LSV), EIS, chronopotentiometry, and chronoamperometry, respectively. The as-prepared electrode was used as the working electrode, platinum mesh as the counter electrode, and Ag/AgCl (saturated KCl) electrode as the reference electrode. Electrochemical impedance was measured at the frequency ranging from 0.01 Hz to 100 kHz with a 5 mV amplitude at the open circuit potential. The obtained potentials were normalized to a reversible hydrogen electrode (RHE) according to eq. (S2).

$$E_{RHE} = E_{Ag/AgCl} + 0.197V + 0.059pH \quad \text{(S2)}$$

The kinetic parameters were calculated from the corresponding LSV curves by the Tafel equation ($\eta = a + b\lg j$, where $\eta$ is the overpotential of the current density 1 A $cm^{-2}$ in the current case, $b$ is the Tafel slope, and $j$ is the current density).

Supercapacitor Test.

The cyclic voltammetry, electrochemical impedance spectroscopy (EIS), galvanostatic charge/discharge properties, and the stability of the electrodes were evaluated using the electrochemical workstation. An asymmetric supercapacitor HS-Te-NiCo-LDH/NiO/NF//AC/NF was assembled using the title electrode (HS-Te-NiCo-LDH/NiO/NF) as the positive electrode and the self-made activated carbon (AC) electrode as the negative electrode. The AC electrode was made by pressing the mixture containing 80 wt % AC, 7.5 wt % carbon black, and 7.5 wt % polytetrafluoroethylene (PTFE) and 5% sodium carboxymethylcellulose (CMC-Na) (add some water to make the ink) onto the NF (current collector), and was dried at 60°C for 24 h before use. The asymmetric supercapacitor was measured by cyclic voltammetry (CV) and galvanostatic charge/discharge (GCD) using the electrochemical workstation in 2 mol $L^{-1}$ KOH solution. Energy (E) and power (P) densities were calculated based on specific capacity by using the eq. (S3) and (S4),

$$E = \frac{1}{7.2} C V^2 \; Wh\; kg^{-1} \quad \text{(S3)}$$

$$P = \frac{3600E}{t} \; W\; kg^{-1} \quad \text{(S4)}$$

where $C$ is the specific capacity of the full cell, $V$ and $t$ are the operating voltage and the discharge time, respectively.

The charge between the two electrodes of the asymmetric supercapacitor was balanced according to the principle $q^{+}=q^{-}$ for the sake of optimum performance prior to the GCD investigation.

**DFT calculations**

Density functional theory (DFT) calculations were performed using the Cambridge Sequential Total Energy Package (CASTEP).[5] Electron-ion interactions were modeled by projector augmented wave (PAW) potentials.[6] Exchange and correlation effects for structural relaxation were approximated by generalized gradient approximation (GGA) using the Perdew-Burke-Ernzerhof (PBE) functional.[6, 7] The Vanderbilt ultrasoft pseudopotential[3] was used with a cutoff energy of 450 eV. Geometric convergence tolerances were set for maximum force of 0.03 eV/Å , maximum energy change of $10^{-5}$ eV/atom, maximum displacement of 0.001 Å and maximum stress of 0.5 GPa. Density mixing electronic minimisation was implemented and the self-consistent field (SCF) tolerance was set to ‘‘fine’’ with high accuracy of $10^{-6}$ eV/atom for energy convergence. K-points were sampled under the Monkhorst-Pack scheme for Brillouin-zone integration.[8] The corresponding HS-Te-NiCo-LDH (001) surface model is shown in Figure S12, where the atomic ratio of Ni:Co:Te was approximately set to 1.3:1:0.01. The atomic structures for all models were relaxed with self-consistency accuracy of $10^{-4}$ eV for electronic loops until the forces on all atoms were < 0.02 eV/Å.

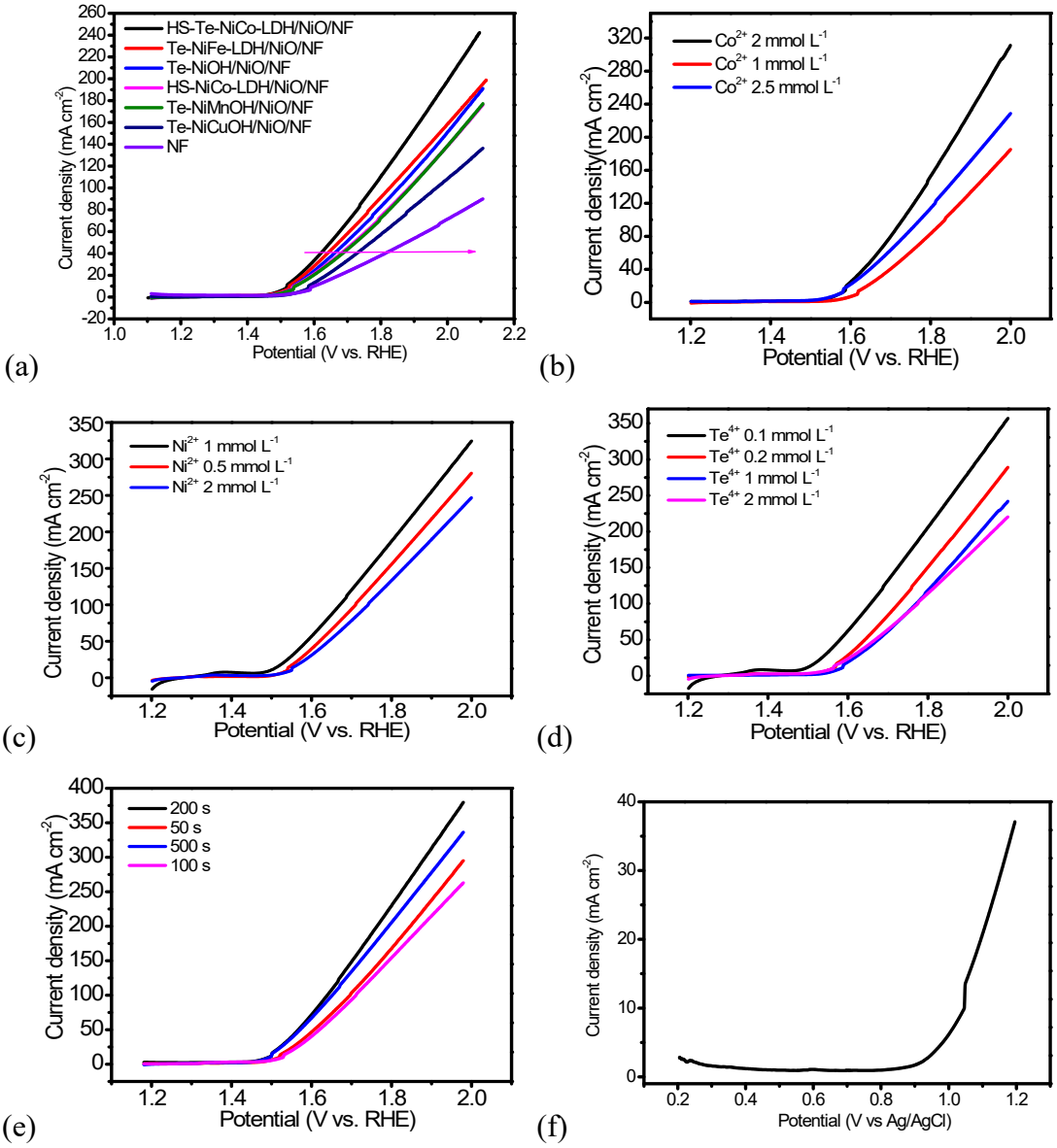


**Figure S1**. (a) LSV curves of the seven samples in 1 M KOH with 5 mV $s^{-1}$ (all metal salts were nitrates, and concentration was 1 mmol $L^{-1}$, electroplating 100 s). (b) LSV curves of HS-Te-NiCo-LDH/NiO/NF with different precursor $Co(NO_3)_2{\cdot}6H_2O$ in the electrolyte, $Ni(NO_3)_2{\cdot}6H_2O$ (1 mmol $L^{-1}$), $TeO_2$ (0.2 mmol $L^{-1}$) and electroplating time of 200 s (5 mV $s^{-1}$ in 1 mol $L^{-1}$ KOH). (c) LSV curves of HS-Te-NiCo-LDH/NiO/NF with different precursor $Ni(NO_3)_2{\cdot}6H_2O$ in the electrolyte, $Co(NO_3)_2{\cdot}6H_2O$ (2 mmol $L^{-1}$), $TeO_2$ (0.2 mmol $L^{-1}$) and electroplating time of 200 s (5 mV $s^{-1}$ in 1 mol $L^{-1}$ KOH). (d) LSV curves of HS-Te-NiCo-LDH/NiO/NF with different precursor $TeO_2$ in the electrolyte, $Co(NO_3)_2{\cdot}6H_2O$ (2 mmol $L^{-1}$), $Ni(NO_3)_2{\cdot}6H_2O$ (1 mmol $L^{-1}$) and electroplating time of 200 s (5 mV $s^{-1}$ in 1 mol $L^{-1}$ KOH). (e) LSV curves of HS-Te-NiCo-LDH/NiO/NF with different electroplating time, $Co(NO_3)_2{\cdot}6H_2O$ (2 mmol $L^{-1}$), $Ni(NO_3)_2{\cdot}6H_2O$ (1 mmol $L^{-1}$) and $TeO_2$ (0.1 mmol

$L^{-1}$). (f) Preparation of the final sample by DOBT-directed anodic electrodeposition by above optimal conditions. In addition, contrast samples without $TeO_2$ was also synthesized denoted as HS-NiCo-LDH/NiO/NF. All the samples were prepared and tested under the same conditions.

A series of samples containing different elements were synthesized (all metal salts are nitrates, and 1 mmol $L^{-1}$, electroplating 100 s) and their OER performances were also studied as shown in Figure S1a. It can be found that the HS-Te-NiCo-LDH/NiO/NF sample provided higher OER activity, suggesting that the introduction of Te has improved OER performance significantly. This may be due to the special characteristics of Te: lower electronegativity (2.1), higher conductivity (~1000 S $m^{-1}$), higher covalent character,[9-12] and possible good synergy with NiCo components.

In order to optimize the HS-Te-NiCo-LDH/NiO/NF electrode, different precursor cobalt ions (1, 2, 2.5 mmol $L^{-1}$) were chosen to prepare the electrolytes, where the concentrations of Te and Ni ions keep at 1 mmol $L^{-1}$, the electrodeposition times keep at 200 s and the synthesized samples were treated by LSV. The linear sweep voltammetry (LSV) curves of these samples were shown in Figure S1b. The results indicated that the 2 mmol $L^{-1}$ cobalt ions sample exhibited better OER performance with higher current density at the same potential during the LSV testing. The 2.5 mmol $L^{-1}$ cobalt ions sample shows good OER performance at first, but with the increase of potential the current density reduced significantly. So 2 mmol $L^{-1}$ cobalt ions was chosen as the optimal concentration. As known, the incorporation of cobalt ions to the electrodeposition solution can produce α-phase nickel-cobalt hydroxide structures with significantly higher OER performance.[13, 14] As instructed by Q. Li, $Co^{2+}$ ion could be easily deposited in the hydroxide form, and the slow $Ni^{2+}$ deposition could be accelerated by $Co^{2+}$ hydroxide to form LDH structure with certain chemical compositions.[13] In our work, the NF substrate provided enough space for the faster growth of hydroxide, so that most of the hydroxides directly nucleated at the surface of deposited hydroxide, which finally led to a large mass loading of hydroxide nanosheets on NF substrate.[13] Otherwise, for the electrode, a maximum OER efficiency is obtained for a proportion of 2:1 (Co:Ni) due to the better conductivity of

Co in the OER process.[15] This may be a result of the typically higher conductivity or higher degree of oxidation of $Ni(OH)_2$ upon the addition of cobalt to the structure.[15]

Figure S1c shows the LSV curves of samples containing different precursor nickel ions (0.5, 1, and 2 mmol $L^{-1}$, keep Te and Co ions at 1 mmol $L^{-1}$ and 2 mmol $L^{-1}$, respectively, electrodeposition time 200 s). As displayed in Figure S1c, the 1 mmol $L^{-1}$ precursor nickel ions sample shows smallest initial potential and higher current density, indicating a better OER performance than others. So 1 mmol $L^{-1}$ precursor nickel ions was chosen as the optimal concentration. As illustrated in Fig S1b, the ratio of Co and Ni 2:1 gave the maximum OER efficiency.

Four precursor tellurium ions concentration (0.1, 0.2, 1, and 2 mmol $L^{-1}$) were used to carry out the single factor experiments (keeping Ni and Co ions at 1 mmol $L^{-1}$ and 2 mmol $L^{-1}$, respectively; electrodeposition time 200 s). From the LSV curves (Figure S1d), it was found that containing 0.1 mmol $L^{-1}$ precursor tellurium sample is superior to others for OER. Increasing the concentration of tellurium ions, the OER activity was reduce. The sample without tellurium ions also shows poor OER performance. This phenomenon just makes sure that the tellurium ion was not electrochemically active which just can stabilize the α-phase of NiCo-LDH. Then, the amount of Te doping should be keep as low as possible.

The samples with different electroplating times were synthesized by changing the scanning speed. The LSV curves of them (Figure S1e) showed that 200 s were the optimal electrodeposition time. A too short electrodeposition time means a thinner active layer and shortage active sites. And a too long deposition time means thicker active layer agglomerating, which would reduce the conductivity and thus the activity of the electrode.[16, 17]

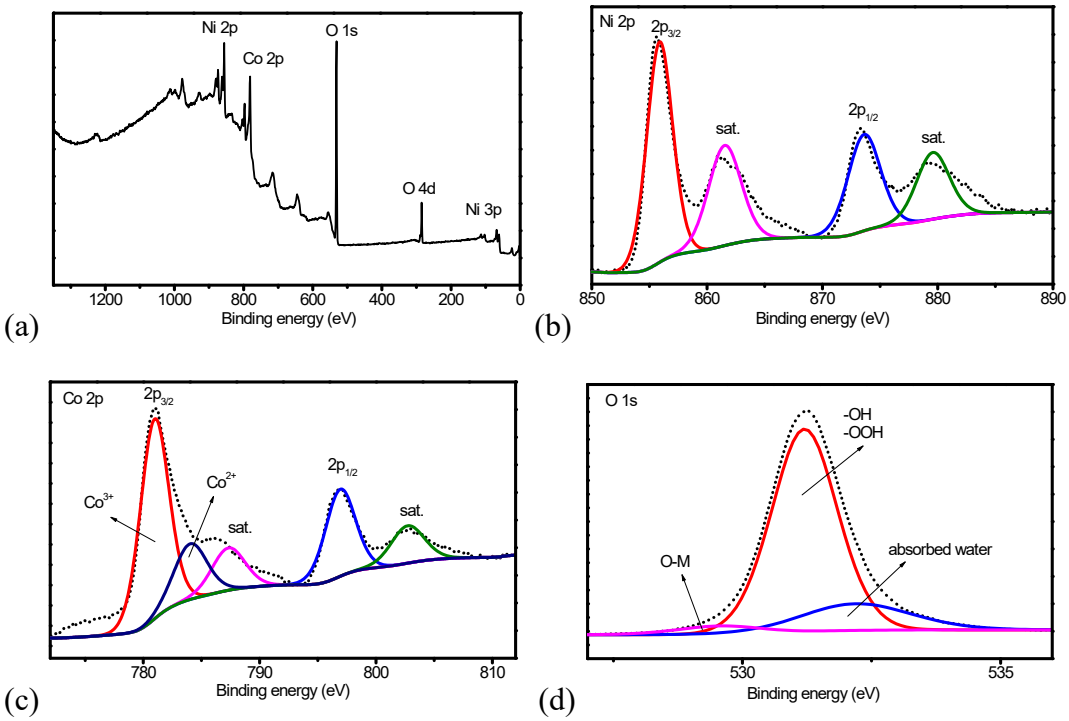


**Figure S2** (a) XPS spectrum of the HS-NiCo-LDH full spectrum, enlarged XPS spectra of (b) Ni 2p, (c) Co 2p and (d) O 1s.

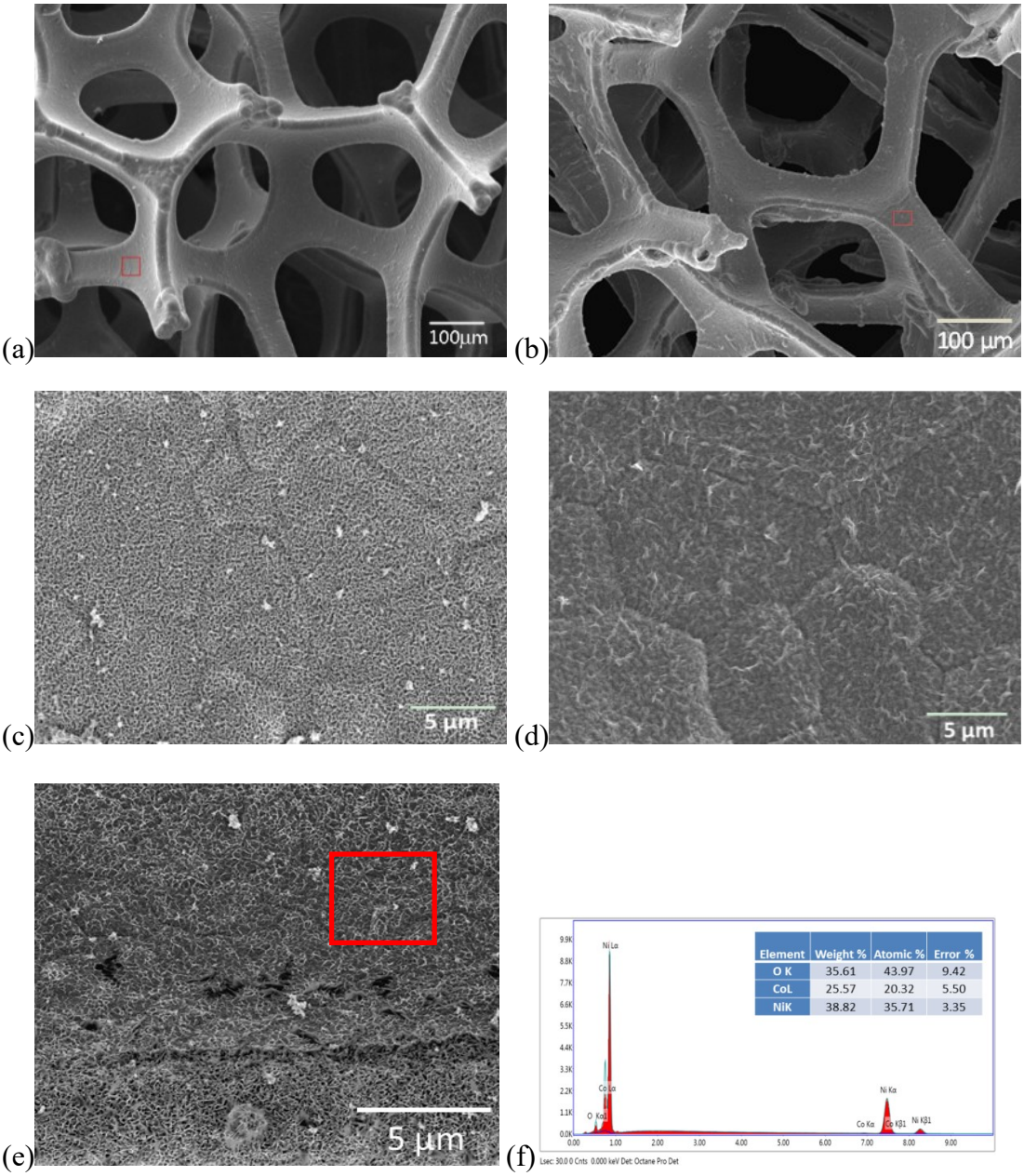


**Figure S3** SEM images of the bare NF (a), HS-Te-NiCo-LDH/NiO/NF (b), Enlarged SEM images of HS-Te-NiCo-LDH/NiO/NF (c), Te-NiCo-LDH/NF (d) and HS-NiCo-LDH/NiO/NF (e). And EDS image of HS-NiCo-LDH/NiO/NF (f).

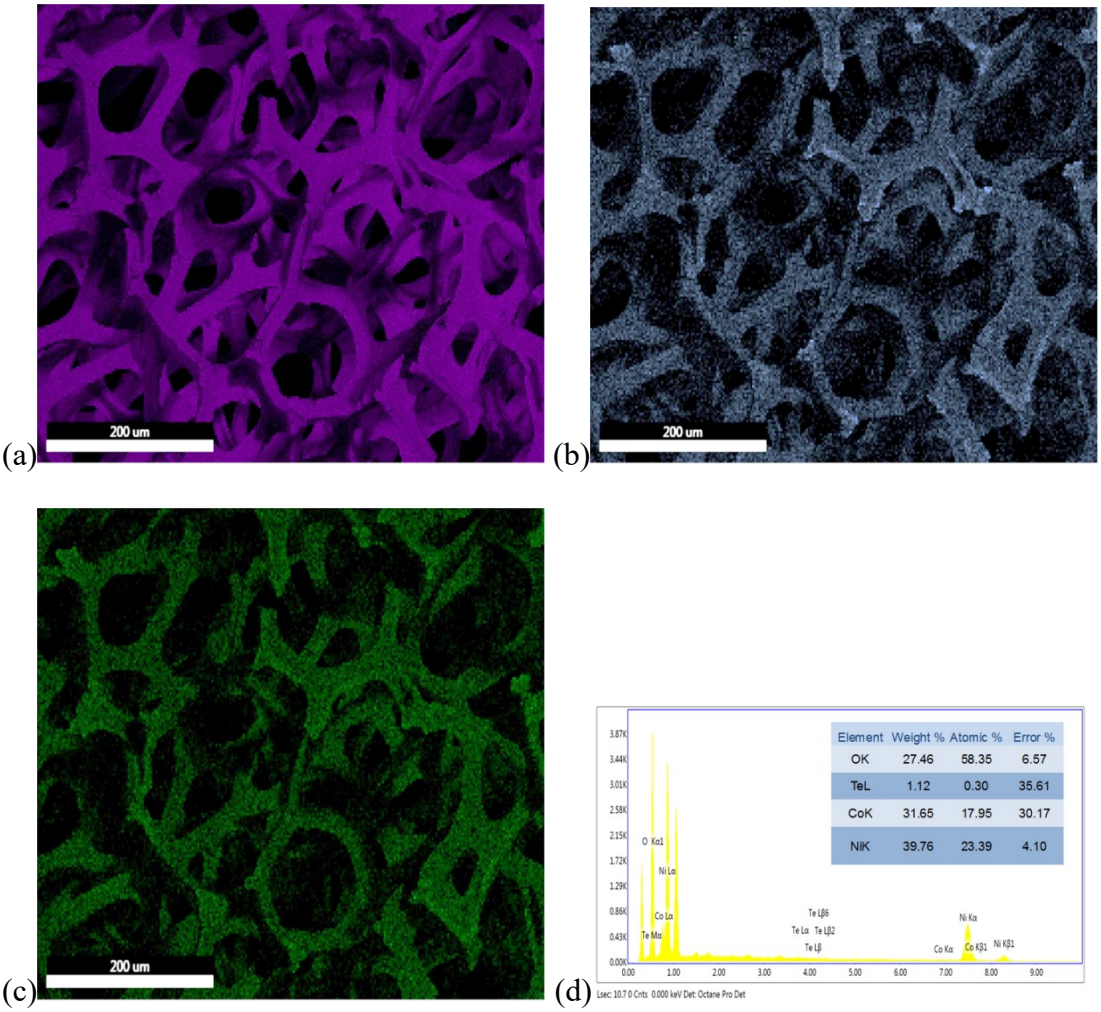


**Figure S4** EDS mappings and point for HS-Te-NiCo-LDH/NiO/NF, Ni (a), Te (b), Co (c) elements and (d) point analysis of HS-Te-NiCo-LDH.

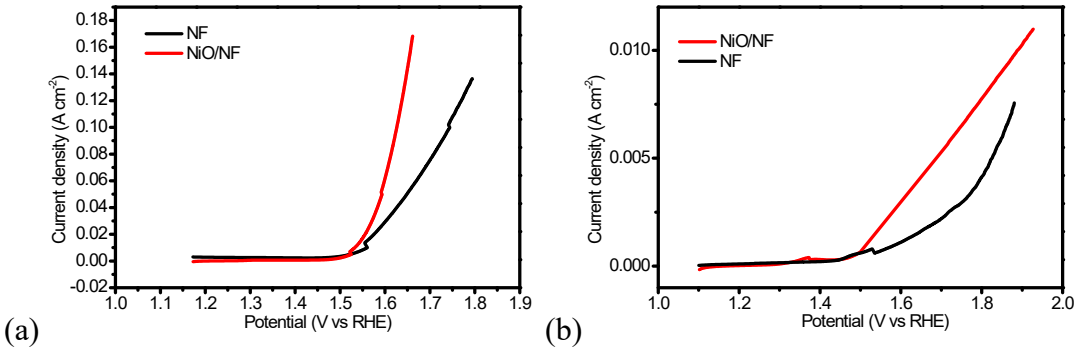


**Figure S5** LSV curves of NiO/NF and NF. (a)1 mol $L^{-1}$ KOH, (b) 0.1 mol $L^{-1}$ KOH.

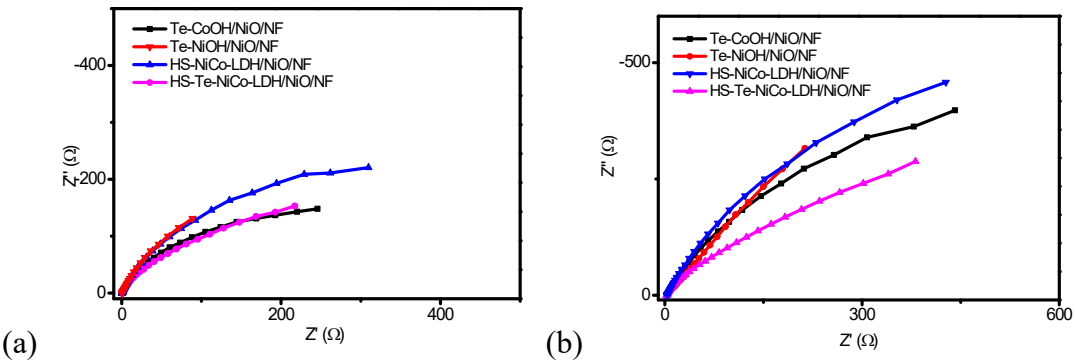


**Figure S6** Nyquist plots of HS-Te-NiCo-LDH/NiO/NF, Te-NiOH/NiO/NF, HS-NiCo-LDH/NiO/NF and Te-CoOH/NiO/NF electrodes obtained at the open circuit potential with the frequency ranging from 0.01 Hz to 100 kHz in 1 mol $L^{-1}$ (a) and 0.1 mol $L^{-1}$ KOH (b) aqueous solution, respectively.

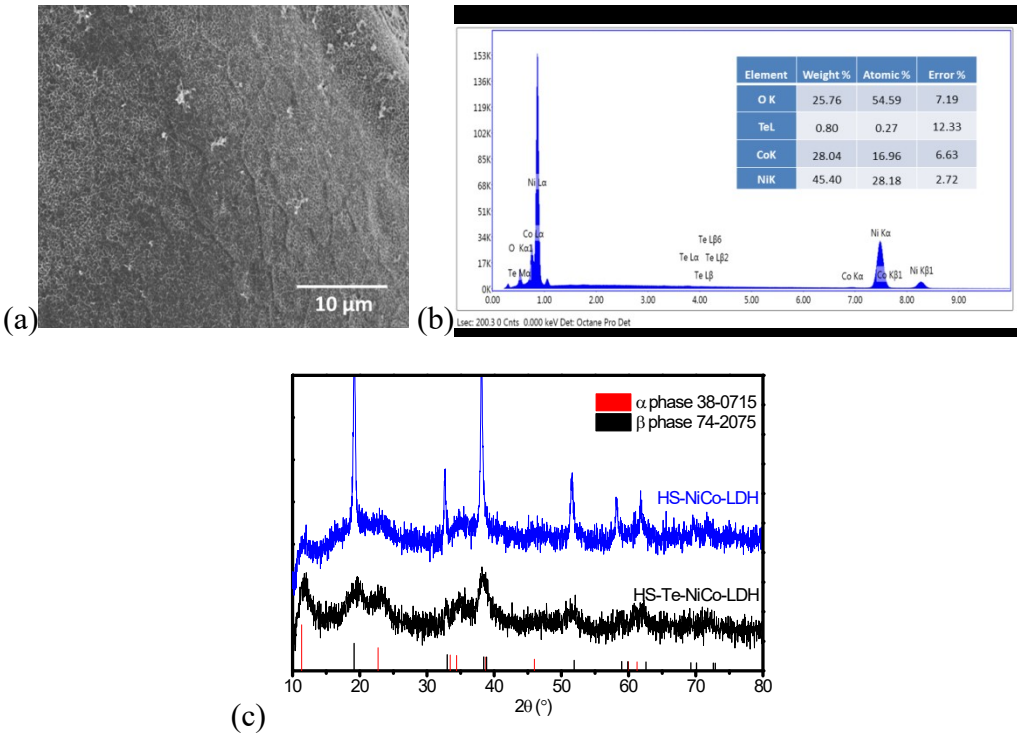


**Figure S7** SEM and corresponding EDS image of HS-Te-NiCo-LDH ultrasonic stripping product form the NiO/NF after 24 h OER test (a,b). XRD pattern of HS-Te-NiCo-LDH and HS-NiCo-LDH ultrasonic stripping product form the NiO/NF after 24 h OER test (c).

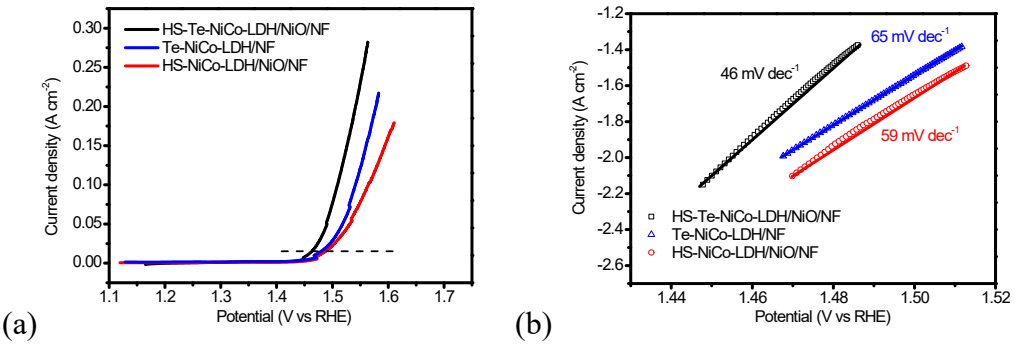


**Figure S8** (a) LSV curves of HS-Te-NiCo-LDH/NiO/NF, Te-NiCo-LDH/NF and HS-NiCo-LDH/NiO/NF electrodes in 1 mol $L^{-1}$ KOH solutions at 5 mV $s^{-1}$ with 95% iR-compensations after 24 h run, (b) Tafel plots in 1 mol $L^{-1}$ KOH at 2 mV $s^{-1}$.

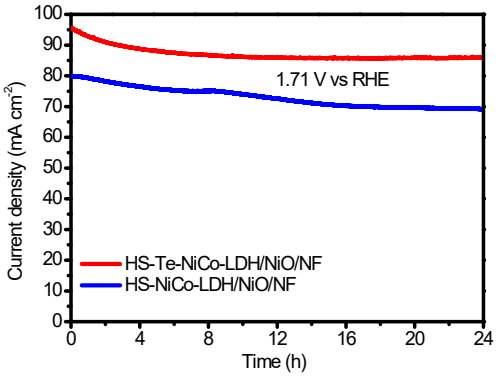


**Figure S9** Chronopotentiometric curves of HS-Te-NiCo-LDH/NiO/NF, and HS-NiCo-LDH/NiO/NF in 1 mol $L^{-1}$ KOH at the same potential of 1.71 V.

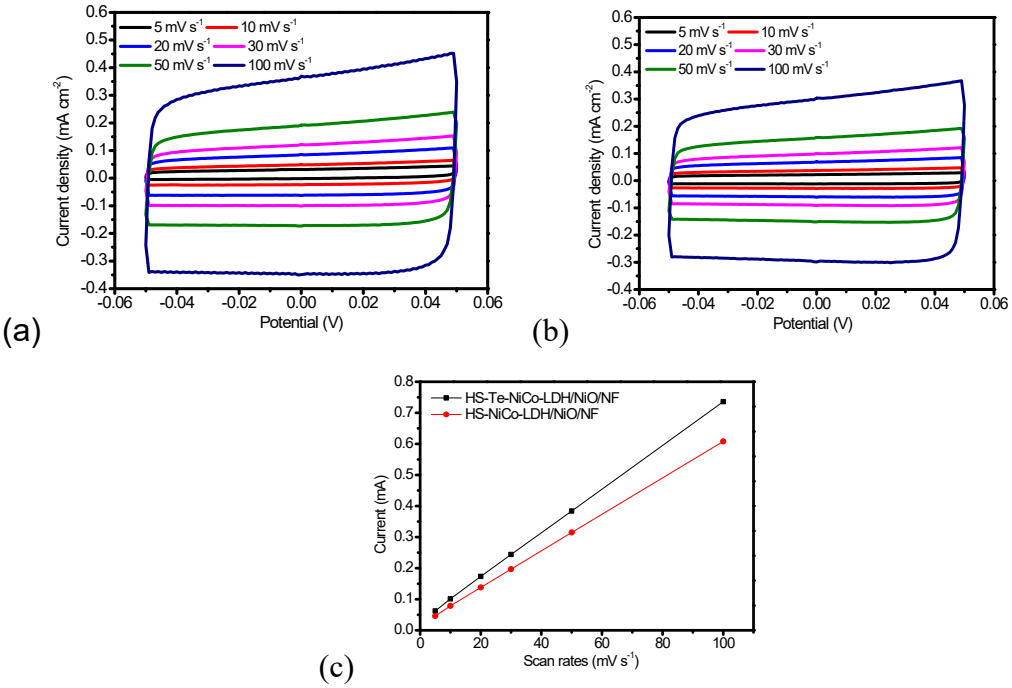


**Figure S10** Double-layer capacitance detected for testing the electrochemically active surface area of the catalysts. (a,b) CVs of the HS-Te-NiCo-LDH/NiO/NF and HS-NiCo-LDH/NiO/NF measured in non-Faradaic potential window at 5, 10, 20, 30, 50 and 100 mV $s^{-1}$. (c) The average value of the absolute anodic currents at 0 V vs. Ag/AgCl was plotted as a function of scan rate. The double-layer capacitances of these catalysts were calculated from the slope of the fitting lines. and they are 0.0071 and 0.0059 F for HS-Te-NiCo-LDH/NiO/NF and HS-NiCo-LDH/NiO/NF, respectively.

The EASSA is calculated by measuring the non-Faradaic capacitive current associated with double-layer charging using cyclic voltammetry within the potential window from -0.05 to 0.05 V (vs Ag/AgCl). In this region all currents were assumed to be due to the capacitive charging. The following equation explains the relationship of scan rate, charging current and double-layer capacitance, where v is the scan rate, $i_C$ is the charging current and $C_{DL}$ is the electrochemical double-layer capacitance [18]. $i_C = v \cdot C_{DL}$

The charging currents were plotted as a function of scan rates (Figure S10e). The dependence of the current on the scan rate is almost linear for the two catalysts, which is in accordance with the capacitive charging behavior.

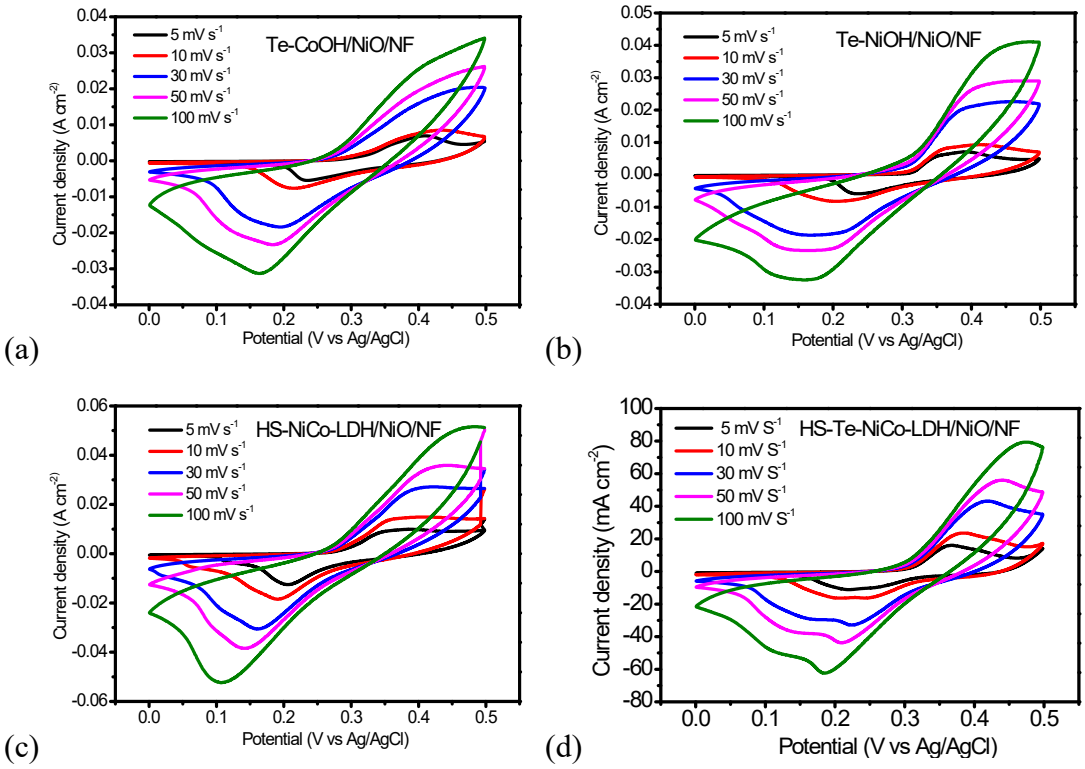


**Figure S11** CV curves of Te-CoOH/NiO/NF (a), Te-NiOH/NiO/NF (b), HS-NiCo-LDH/NiO/NF (c) and HS-Te-NiCo-LDH/NiO/NF (d) electrodes measured at different scan rates.

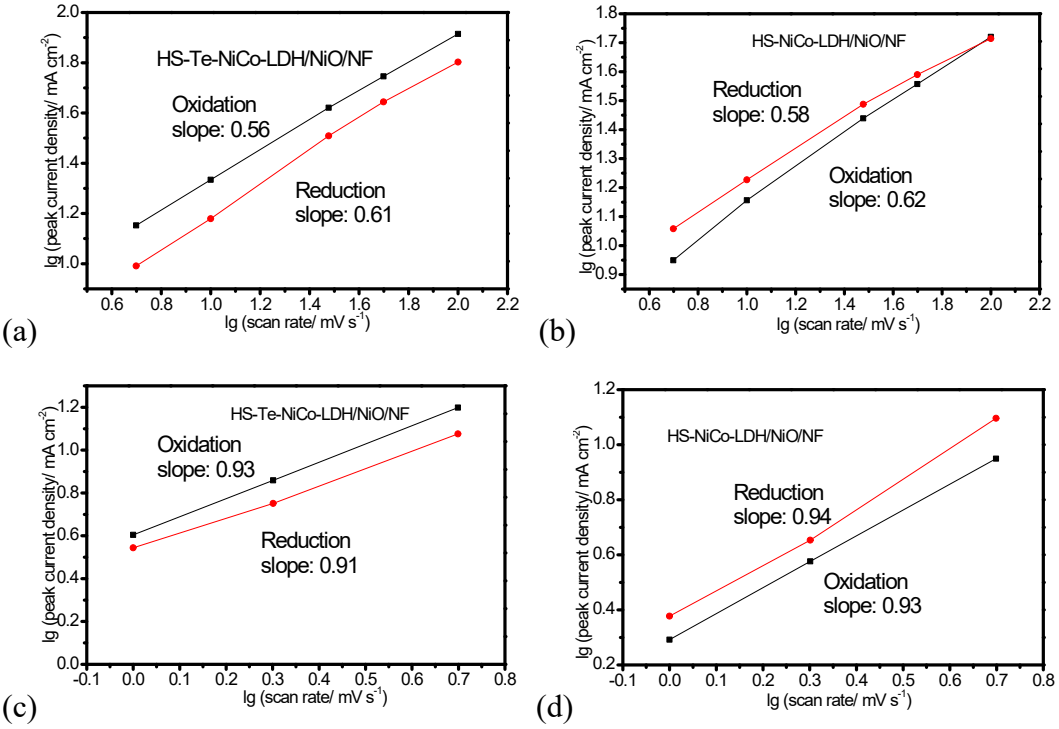


**Figure S12** The relationship between peak current densities (oxidation and reduction) and scan rates for the HS-Te-NiCo-LDH/NiO/NF (a, c) and HS-NiCo-LDH/NiO/NF (b, d). In general, the peak current density i obeys a power-law relationship with the sweep rate v[19] ($i = av^b$) in which the parameter b is determined from the slope of the linear plot of lg*i* vs lgv. If $b = 1.0$, the kinetics is dominated by surface electrochemical reaction processes. If $a = 0.5$, the kinetics are limited by surface electrochemical reaction processes.

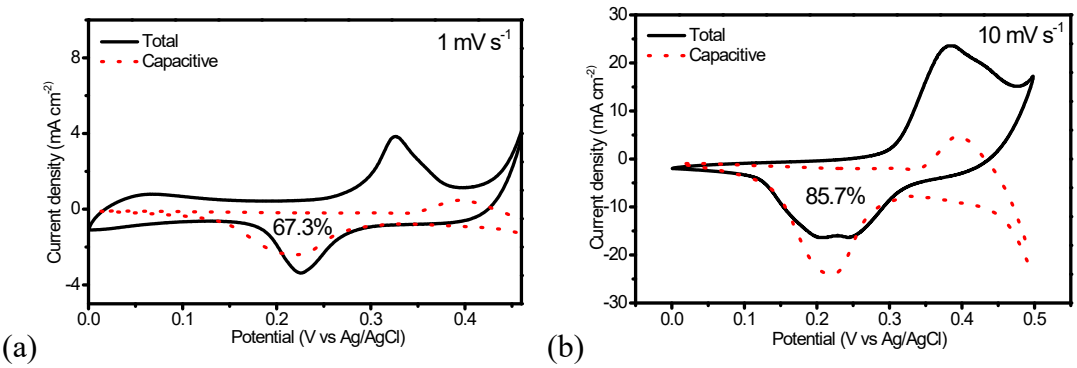


**Figure S13** The capacitive contribution to total charge storage of the HS-Te-NiCo-LDH/NiO/NF electrode at different scan rates of (a) 1 mV $s^{-1}$ and (b) 10 mV $s^{-1}$. The 67.3% and 85.7% means the percentage of capacitive in the total charge storage.

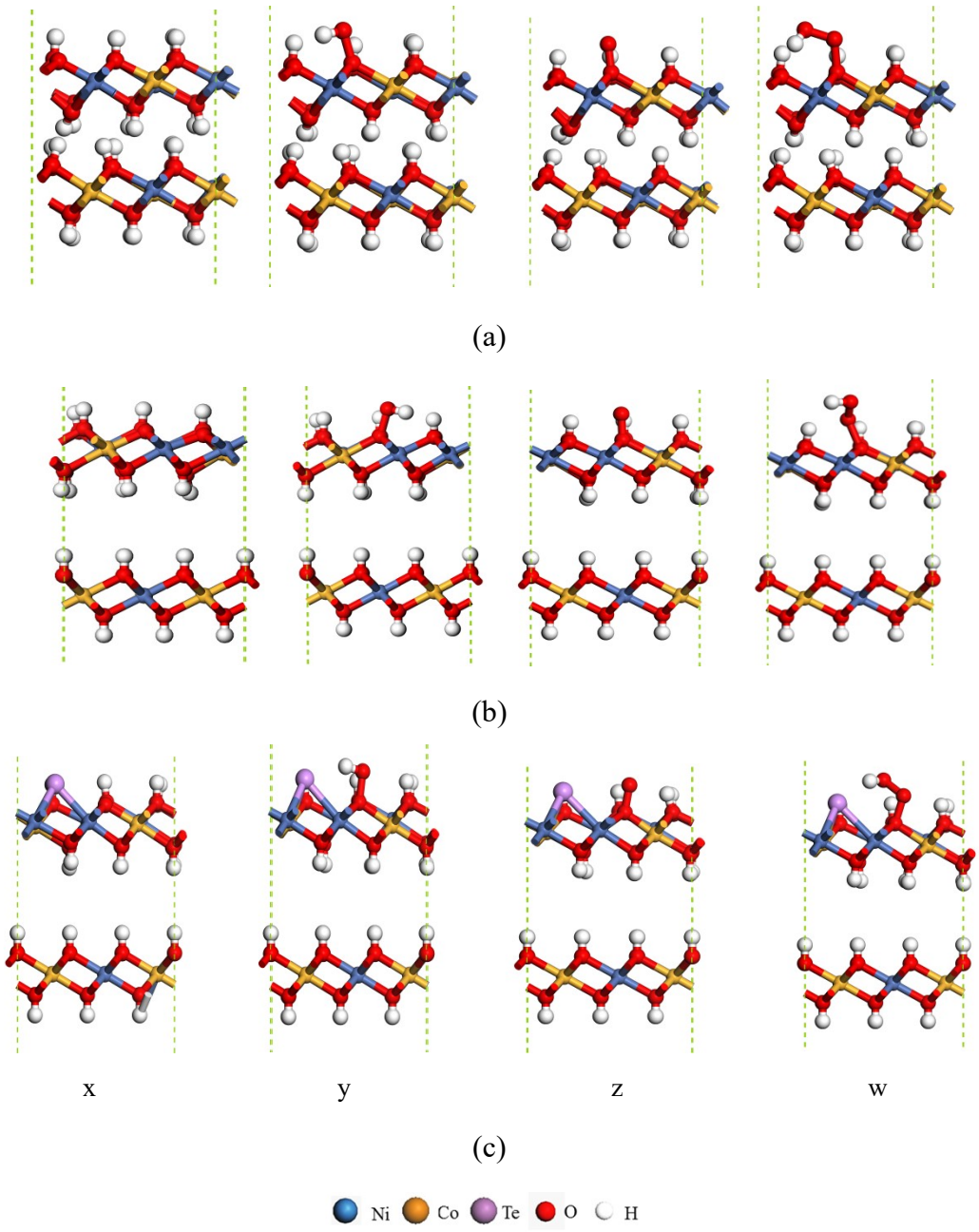


**Figure S14** Atomic structures of (a) β-NiCo-LDH, α-NiCo-LDH (b) and α-Te-NiCo-LDH (c, corresponding to HS-Te-NiCo-LDH/NiO/NF) unit cell (001) surface model. The (x~w) demonstrated the four steps for the free energy of the two materials.

The free energy was calculated using the Eq. S5[20, 21]:

$$G = E + ZPE - TS \qquad \text{(Eq. S5)}$$

Where, $G$, $E$, $ZPE$, and $TS$ were the free energy, total energy from DFT calculations, zero-point energy, and entropic contributions ($T$ was set to be

298K), respectively.[21] *ZPE* could be derived after frequency calculation by Eq. S6:

$$ZPE = \frac{1}{2}\sum hv_i \quad \text{(Eq. S6)}$$

*TS* values of $H_2O$ and $H_2$ were from previous reports.[5, 21, 22] And the *TS* values of adsorbed species were calculated after obtaining the vibrational frequencies (Eq. S7):

$$TS_v = k_B T\left[\sum_K \ln\left(\frac{1}{1-e^{-hv/k_B T}}\right) + \sum_K \frac{hv}{k_B T}\frac{1}{(e^{hv/k_B T}-1)} + 1\right] \quad \text{(Eq. S7)}$$

According to the previous study on the OER pathway in alkaline media,[22] the OER pathway was described as the adsorption of successive intermediate species on the catalyst and the relevant reaction energies were as follows (Eq. S8 ~ Eq. S11):

$$OH^- + cat \rightarrow \cdot OH\text{-}cat + e^- \quad \text{(Eq. S8)}$$

$$\cdot OH\text{-}cat + OH^- \rightarrow \cdot O\text{-}cat + H_2O + e^- \quad \text{(Eq. S9)}$$

$$\cdot O\text{-}cat + OH^- \rightarrow \cdot OOH\text{-}cat + e^- \quad \text{(Eq. S10)}$$

$$\cdot OOH\text{-}cat + OH^- \rightarrow O_2\uparrow + H_2O + e^- \quad \text{(Eq. S11)}$$

The *cat* represented the active site when OER occurred. The $\cdot OH$, $\cdot O$, $\cdot OOH$ represented the intermediate species adsorbed on the active sites. In order to evaluate OER activity, we calculated the free energy ($\Delta G_1$~$\Delta G_4$) using the computational standard hydrogen electrode model. The free energy calculation could be obtained as follows:

$$\Delta G_1 = G_{OH-cat} - G_{cat} - G_{H_2 0} + {}^1\!/_2 G_{H_2} - eU + K_B ln10 \cdot pH \quad \text{(Eq. S12)}$$

$$\Delta G_2 = G_{O-cat} - G_{OH-cat} + {}^1\!/_2 G_{H_2} - eU + K_B ln10 \cdot pH \quad \text{(Eq. S13)}$$

$$\Delta G_3 = G_{OOH-cat} - G_{O-cat} - G_{H_2 0} + {}^1\!/_2 G_{H_2} - eU + K_B ln10 \cdot pH \quad \text{(Eq. S14)}$$

$$\Delta G_4 = 4.92 - \Delta G_1 - \Delta G_2 - \Delta G_3 \quad \text{(Eq. S15)}$$

It should be noted that $-eU$ represented the free energy changes for one-electron transfer where $U$ was electrode potential represented the standard

hydrogen electrode. For pH ≠ 0, pH affected on free energy could be defined as $-K_BT\cdot\ln 10\cdot pH$, where $K_B$ was Boltzman constant. $\Delta G_4$ was calculated by $4.92-\Delta G_1-\Delta G_2-\Delta G_3$ to avoid calculating the $O_2$ adsorption and desorption. It was known that the DFT calculation might not accurately describe the free energy of $O_2$ molecule in the gas phase and hence we used $H_2O$ and $H_2$ as a reference and from there we extracted the free energy of $O_2$ through the reaction $O_2 + 4(H^+ + e^-) \rightarrow 2H_2O$. The equilibrium potential for this reaction was 1.23 V and since it was a four-electron transfer reaction, the full energy was $4 \times 1.23 = 4.92$ eV. This analysis was based on the scheme developed by Norskov's group.[23] The overpotential of OER in this mechanism was defined as $\eta_{OER} = max(\Delta G_{OER}/e) - 1.23\ V$. [22]

**Table S1** XPS analysis of HS-Te-NiCo-LDH

| Element | Atomic % |
|---|---|
| O 1s | 40.79 |
| Co 2p | 6.47 |
| Ni 2p | 8.9 |
| Te 3d | 0.09 |

**Table S2** Electrochemical parameters obtained from EIS in KOH solutions

| Catalysts | Rs (Ω) | Rct (Ω) |
|---|---|---|
| | 1 mol $L^{-1}$/0.1 mol $L^{-1}$ | 1 mol $L^{-1}$/ 0.1 mol $L^{-1}$ |
| HS-Te-NiCo-LDH/NiO/NF | 0.55/0.57 | 1.13/1.26 |
| HS-NiCo-LDH/NiO/NF | 0.76/0.67 | 1.28/1.57 |
| Te-NiOH/NiO/NF | 0.73/0.78 | 1.42/1.97 |
| Te-CoOH/NiO/NF | 0.74/0.79 | 2.06/2.31 |

Equivalent circuit of Figure S6.

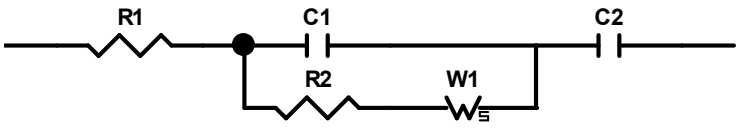

**Table S3** Comparisons of the electrocatalytic activity of optimized HS-Te-NiCo-LDH/NiO/NF with some other representative OER catalysts measured in 1 mol $L^{-1}$ KOH.

| Catalyst | Current density ($mA\ cm^{-2}$) | Overpotential (mV) | Reference |
|---|---|---|---|
| **Ex-FeN-MC** | 10 | 250 | [24] |
| **Co/MnO@GC-700** | 10 | 358 | [25] |
| **$(Co_4Mn_1)Se_2$** | 10 | 274 | [26] |
| **$Co_3O_{4-x}$** | 10 | 330 | [27] |
| **NiCo-LDH** | 10 | 280 | [28] |
| **$Co_1Mn_1CH$/NF** | 30 | 294 | [29] |
| **$V_x$ -NiFe-LDH** | 10 | 254 | [30] |
| **FeNi LDH** | 10 | 250 | [31] |
| **Pt/NiFe-LDH** | 10 | 261 | [32] |
| **CoFe-LDH** | 10 | 270 | [33] |
| **$CoNi_2S_4$@NiMn-LDH** | 10 | 272 | [34] |
| **HS-Te-NiCo-LDH/NiO/NF** | **10** | **221** | **Present work** |

**Table S4** OER overpotentials (mV) of the samples at different current densities in 1 mol $L^{-1}$ KOH.

| Sample | Overpotential (mV) | | |
|---|---|---|---|
| | 10 mA $cm^{-2}$ | 20 mA $cm^{-2}$ | 100 mA $cm^{-2}$ |
| HS-Te-NiCo-LDH/NiO/NF | 221 | 229 | 267 |
| HS-NiCo-LDH/NiO/NF | 251 | 264 | 325 |
| Te-NiOH/NiO/NF | 270 | 298 | 381 |
| Te-CoOH/NiO/NF | 279 | 308 | 417 |
| NF | 321 | 341 | 511 |

**Table S5** Comparison of the supercapacitive performances of HS-Te-NiCo-LDH/NiO/NF with some other Ni-based electrodes

| Electrode | Current density (A $g^{-1}$) | Specific capacity | Stability (cycling)/(retention) | References |
|---|---|---|---|---|
| NiSe–G | 1 | 1280 F $g^{-1}$ | 2500/98% | 35 |
| NiCo-LDH | 1 | 217.5 mA h $g^{-1}$ | 10000/90% | 36 |
| $Co_3O_4$@CoNi-LDH | 0.5 | 2676.9 F $g^{-1}$ | 10000/67.7% | 37 |
| $Ni_3S_4$ | 0.5 | 1797.5 F $g^{-1}$ | 5000/93% | 38 |
| MOF-derived NiCo | 1 | 1676 F $g^{-1}$ | 5000/76.6% | 39 |
| **HS-Te-NiCo-LDH/NiO/NF** | **10** | **650 C $g^{-1}$ (1300 F $g^{-1}$)** | **10000/91%** | **Present work** |

## References


1. S. L. Medway, C. A. Lucas, A. Kowal, R. J. Nichols and D. Johnson, *J. Electroanal. Chem.*, 2006, **587**, 172-181.
2. X.-F. Chuah, C.-T. Hsieh, C.-L. Huang, D. Senthil Raja, H.-W. Lin and S.-Y. Lu, *ACS Appl. Energy Mater.*, 2019, **2**, 743-753.
3. W. J. Dong, Y. J. Song, H. Yoon, G. H. Jung, K. Kim, S. Kim and J.-L. Lee, *Advanced Energy Materials*, 2017, **7**, 1700659.
4. N. Comisso, S. Cattarin, P. Guerriero, L. Mattarozzi, M. Musiani and E. Verlato, *Electrochim. Acta*, 2016, **200**, 259-267.
5. C. Guan, W. Xiao, H. Wu, X. Liu, W. Zang, H. Zhang, J. Ding, Y. P. Feng, S. J. Pennycook and J. Wang, *Nano Energy*, 2018, **48**, 73-80.
6. P. E. Blöchl, *Phys. Rev. B*, 1994, **50**, 17953-17979.
7. J. P. Perdew, K. Burke and M. Ernzerhof, *Phys. Rev. Lett.*, 1996, **77**, 3865-3868.
8. H. J. Monkhorst and J. D. Pack, *Phys. Rev. B*, 1976, **13**, 5188-5192.
9. Q. Wang, J. Zhu, H. Wang, S. Yu and X. Wu, *Mater. Today Energy*, 2019, **11**, 199-210.
10. J. Cao, M. Safdar, Z. Wang and J. He, *J. Mater. Chem. A*, 2013, **1**, 10024-10029.
11. C. Kartick, K. Paramita and M. Rashmi, *Electrochim. Acta*, 2019, **318**, 901-912.
12. U. De Silva, J. Masud, N. Zhang, Y. Hong, W. P. R. Liyanage, M. Asle Zaeem and M. Nath, *J. Mater. Chem. A*, 2018, **6**, 7608-7622.
13. H. Chen, F. Cai, Y. Kang, S. Zeng, M. Chen and Q. Li, *ACS Appl. Mater. Inter.*, 2014, **6**, 19630-19637.
14. A. Balram, H. F. Zhang and S. Santhanagopalan, *ACS Appl. Mater. Inter.*, 2017, **9**, 28355-28365.
15. A. Cressent, V. Pralong, A. Audemer, J.-B. Leriche, A. Delahaye-Vidal and J.-M. Tarascon, *Solid State Sci.*, 2001, **3**, 65-80.
16. P. Ganesan, A. Sivanantham and S. Shanmugam, *ACS Appl. Mater. Inter.*, 2017, **9**, 12416-12426.
17. C. G. Morales-Guio, L. Liardet and X. Hu, *J. Am. Chem. Soc.*, 2016, **138**, 8946-8957.
18. C. Chang, L. Zhang, C. W. Hsu, X. F. Chuah and S. Y. Lu, *ACS Appl. Mater. Inter.*, 2018, **10**, 417-426.
19. T. Brezesinski, J. Wang, S. H. Tolbert and B. Dunn, *Nat. Mater.*, 2010, **9**, 146.
20. R. M. A. Khalil, F. Hussain, M. I. Hussain, A. Parveen, M. Imran, G. Murtaza, M. A. Sattar, A. M. Rana and S. Kim, *J. Alloys Compd.*, 2020, **827**, 154255.
21. M. Li, L. Zhang, Q. Xu, J. Niu and Z. Xia, *J. Catal.*, 2014, **314**, 66-72.
22. I. C. Man, H.-Y. Su, F. Calle-Vallejo, H. A. Hansen, J. I. Martínez, N. G. Inoglu, J. Kitchin, T. F. Jaramillo, J. K. Nørskov and J. Rossmeisl, *ChemCatChem*, 2011, **3**, 1159-1165.
23. B. Hammer, L. B. Hansen and J. K. Nørskov, *Phys. Rev. B*, 1999, **59**, 7413-7421.
24. R. Akram, M. A. Ud Din, S. U. Dar, A. Arshad, W. Liu, Z. Wu and D. Wu, *Nanoscale*, 2018, **10**, 5658-5666.
25. J. Xu, H. Zhang, P. Xu, R. Wang, Y. Tong, Q. Lu and F. Gao, *Nanoscale*, 2018, **10**, 13702-13712.
26. X. Zhao, X. Li, Y. Yan, Y. Xing, S. Lu, L. Zhao, S. Zhou, Z. Peng and J. Zeng, *Appl. Catal., B: Environ.*, 2018, **236**, 569-575.
27. L. Ma, S. Chen, Z. Pei, H. Li, Z. Wang, Z. Liu, Z. Tang, J. A. Zapien and C. Zhi, *ACS Nano*, 2018,

**12**, 8597-8605.
28. J. Shi, N. Du, W. Zheng, X. Li, Y. Dai and G. He, *Chem. Eng. J.*, 2017, **327**, 9-17.
29. T. Tang, W. J. Jiang, S. Niu, N. Liu, H. Luo, Y. Y. Chen, S. F. Jin, F. Gao, L. J. Wan and J. S. Hu, *J. Am. Chem. Soc.*, 2017, **139**, 8320-8328.
30. Y. Kong, Y. Wang, W. Chu and Z. Liu, *J. Alloys Compd.*, 2021, **885**, 160929.
31. Y. Chen, H. Yao, F. Kong, H. Tian, G. Meng, S. Wang, X. Mao, X. Cui, X. Hou and J. Shi, *Appl. Catal., B: Environ.*, 2021, **297**, 120474.
32. Y. Zhao, Y. Gao, Z. Chen, Z. Li, T. Ma, Z. Wu and L. Wang, *Appl. Catal., B: Environ.*, 2021, **297**, 120395.
33. Y. Zhou, J. Hu, D. Li and Q. Gao, *Chem. Commun.*, 2021, **57**, 7653-7656.
34. P. Wang, J. Qi, C. Li, W. Li, T. Wang and C. Liang, *Electrochim. Acta*, 2020, **345**, 136247.
35. B. Kirubasankar, V. Murugadoss, J. Lin, T. Ding, M. Dong, H. Liu, J. Zhang, T. Li, N. Wang, Z. Guo and S. Angaiah, *Nanoscale*, 2018, **10**, 20414-20425.
36. K. Qin, L. Wang, S. Wen, L. Diao, P. Liu, J. Li, L. Ma, C. Shi, C. Zhong, W. Hu, E. Liu and N. Zhao, *J. Mater. Chem. A*, 2018, **6**, 8109-8119.
37. J.-J. Zhou, Q. Li, C. Chen, Y.-L. Li, K. Tao and L. Han, *Chem. Eng. J.*, 2018, **350**, 551-558.
38. H. Wang, M. Liang, D. Duan, W. Shi, Y. Song and Z. Sun, *Chem. Eng. J.*, 2018, **350**, 523-533.
39. A. Jayakumar, R. P. Antony, J. Zhao and J.-M. Lee, *Electrochim. Acta*, 2018, **265**, 336-347.